# Multifunctional Polyfluoride Ionogel-Encapsulated Lithium Anodes for Durable and Safe Pouch Cells under Harsh Conditions

*Ting Li, Anjun Hu,\* Yuanjian Li, Borui Yang, Kun Li, Kai Chen, Jingyun Jiang, Fei Li, Zhi Wei Seh,\* Jian Wang,\* and Jianping Long\**

Lithium metal is environmentally sensitive and highly reactive, especially when coupled with flammable organic electrolytes, which pose critical safety challenges for lithium metal batteries under harsh operational conditions. This study tackles this challenge by constructing an integrated strategy for encapsulating lithium metal with a multifunctional polyfluoride ionogel (PFIGE) through in situ thermal polymerization. Based on the cross-linking network design of hexafluorobutyl methacrylate monomer and 1-butyl-3-lithium bis(trifluoromethylsulfonyl)imide ionic liquid plasticizer, C—F group and TFSI$^-$ anion cooperate to confer excellent water/oxygen barrier properties of the PFIGE. Meanwhile, the fluorinated skeleton optimizes the Li$^+$ flux by regulating anion migration, thereby promoting the formation of stable inorganic-rich interphases and achieving homogeneous lithium deposition. Additionally, the C—F group forms ion—dipole interactions with imidazole cations to achieve dynamic self-healing capabilities, while the condensed-phase physical barrier and gas-phase radical scavenging effect of the pyrolyzed PFIGE synergistically contribute to the battery safety. As a proof-of-concept, PFIGE-integrated Li‖LiNi$_{0.5}$Co$_{0.2}$Mn$_{0.3}$O$_2$ cells demonstrate extended cycling stability at high voltage (4.6 V) and high temperature (80 °C), and a 0.4 Ah-level pouch cell exhibits exceptional resistance to thermal runaway under mechanical/electrical/thermal abuse conditions. This design philosophy presents a paradigm-shifting electrolyte system that significantly enhances the cycle life and safety of lithium metal batteries.

## 1. Introduction

Lithium metal is an ideal anode material for the next-generation high-energy-density batteries owing to its exceptionally high theoretical specific capacity (3860 mAh g$^{-1}$) and lowest electrochemical potential (−3.04 V vs. standard hydrogen electrodes).[1–5] However, its practical application in lithium metal batteries (LMBs) is hindered by environmental sensitivity and high reactivity.[6–8] Lithium metal spontaneously reacts with water molecules to form lithium hydroxide and hydrogen in humid air, and also reacts slowly with nitrogen in dry environments. This chemical instability necessitates stringent requirements for electrode processing, which must be conducted in an inert atmosphere with a dew point below −50 °C, significantly increasing production costs. More critically, the electrochemical behavior of lithium metal is unstable. The heterogeneity and mechanical brittleness of solid electrolyte interphase (SEI) on the surface of lithium metal can lead to uneven distribution of ion flux and local charge accumulation.[9,10] This non-uniform deposition exacerbates the growth

T. Li, A. Hu, B. Yang, K. Li, K. Chen, J. Long
College of Materials and Chemistry & Chemical Engineering (College of Lithium Resources and Lithium Battery Industry)
Chengdu University of Technology
Chengdu 610059, China
E-mail: anjunhu@cdut.edu.cn; longjianping@cdut.cn
J. Wang
Helmholtz Institute Ulm (HIU)
D89081 Ulm, Germany
E-mail: jian.wang@kit.edu

J. Wang
Karlsruhe Institute of Technology (KIT)
D-76021 Karlsruhe, Germany
Y. Li, J. Jiang, Z. W. Seh
Institute of Materials Research and Engineering (IMRE), Agency for Science
Technology and Research (A*STAR) 2 Fusionopolis Way
Innovis #08-03, Singapore 138634, Republic of Singapore
E-mail: sehzw@imre.a-star.edu.sg
F. Li
School of Materials and Energy
University of Electronic Science and Technology of China
Chengdu 610054, China
J. Jiang
School of Materials Science and Engineering
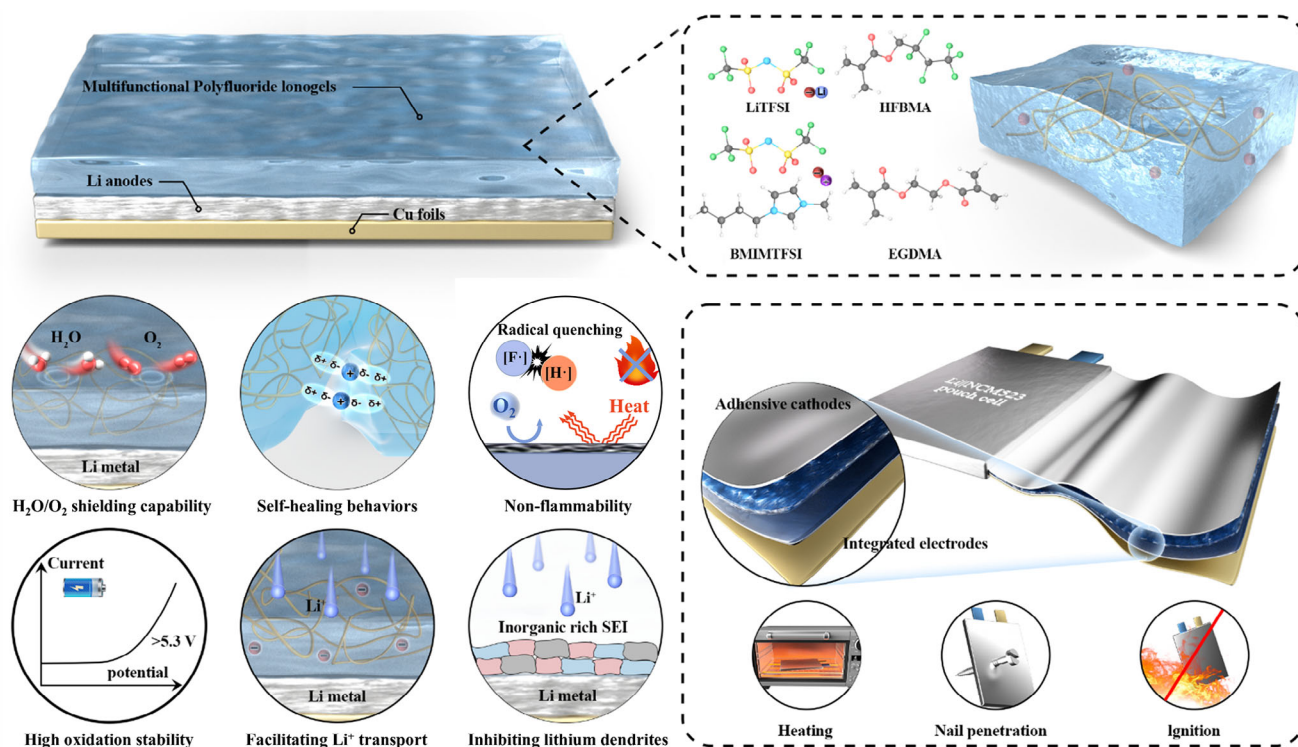Zhengzhou University
Zhengzhou 450001, China

**Figure 1.** Schematic illustration of the multifunctional polyfluoride ionogel-encapsulated lithium anodes. The PFIGE, with its well-designed multi-component structure, exhibits multiple advantageous properties including water/oxygen shielding capability, self-healing behavior, non-flammability, and high oxidation stability. Moreover, it facilitates Li+ transport while effectively suppressing lithium dendrite growth. In the pouch cell design, the integrated PFIGE-encapsulated lithium anode was directly laminated with the cathode, demonstrating excellent safety performance by successfully passing rigorous heating, nail penetration, and ignition tests.

of lithium dendrites and the formation of dead lithium, resulting in rapid performance degration and even internal short circuits.[11–13] Furthermore, when lithium metal is paired with flammable organic electrolytes, these issues become more pronounced, posing significant safety risks under harsh operating conditions.[14–16] These challenges not only affect the long-term stability and safety of LMBs but also limit their widespread application in high-performance energy storage systems.

In light of the complex challenges mentioned above, existing research mostly adopts a "divide and rule" strategy, which struggles to achieve synergistic performance optimization. On one hand, although physical encapsulation layer[17,18] or artificial SEI layer[19,20] can temporarily isolate water/oxygen erosion, they fail to dynamically repair mechanical damage caused by cyclic stress. Thereby, interface ruptures expose fresh lithium surfaces, leading to irreversible side reactions. On the other hand, although electrolyte modification[21,22] can guide uniform lithium deposition, it often lacks flame retardancy or high voltage compatibility. Introducing liquid flame-retardant additives can improve safety but tends to cause concentration polarization due to anion migration, exacerbating the imbalance of electrode dynamics. In addition, conventional inorganic solid electrolytes inhibit dendrite growth through high mechanical strength but sacrifice interfacial contact. In comparison, polymer solid electrolytes, despite their excellent flexibility and interface characteristics, suffer from low room-temperature ionic conductivity and flammability. Other strategies, such as 3D current collectors[23,24]

structured anodes[25] or alloyed anodes[26] can enhance stability but are constrained by cost explosions and process complexity. The prevailing research paradigm essentially stems from the fact that it is difficult for a single functional material to meet multiple requirements simultaneously, such as environmental passivation, interface adaptation, ion conduction, and intrinsic flame retardancy. This functional decoupling directly impedes the long-term stable operation of LMBs under complex working conditions. Therefore, achieving multifunctional coupling at the molecular scale has become a critical technical bottleneck to break through the stability and safety challenges of lithium metal anodes.

In this study, we propose a molecular-level integrated strategy involving the in situ construction of a multifunctional polyfluoride ionogel (PFIGE) encapsulating lithium anodes, effectively integrating the aforementioned advantages (**Figure 1**). Specifically, a polyfluorinated monomer (hexafluorobutyl methacrylate, HFBMA) containing electron-withdrawing groups were selected to form a crosslinked network structure thermally initiated with ethylene glycol dimethacrylate (EGDMA) and filled with 1-butyl-3-lithium bis(trifluoromethylsulfonyl)imide (BMIMTFSI) ionic liquids as plasticizers. Molecular dynamics simulations and density functional theory calculations reveal that the abundant C−F groups, combined with a large number of TFSI− anions, endow the electrolye with excellent water/oxygen shielding properties. Meanwhile, the polyfluorine groups within the polymer backbone can limit anions migration by regulating the weak

**ADVANCED
SCIENCE NEWS**

www.advancedsciencenews.com

**ADVANCED
FUNCTIONAL
MATERIALS**

www.afm-journal.de

intermolecular forces between the polymer network and anions, thereby effectively regulating Li$^+$ flux, promoting enven lithium deposition, and inhibiting the dendrites growth. In addition, the dynamic and reversible ion−dipole interactions between the polymer network and the ionic liquid impart PFIGE with self-healing capabilities, which helps to prolong the battery life. At high temperatures, PFIGE decomposes to release gas-phase free radicals that interrupt the combustion reaction and form a protective char layer, collectively enhancing the battery safety. This approach enables extended cycle life for the Li||LiNi$_{0.5}$Co$_{0.2}$Mn$_{0.3}$O$_2$ cell under both high voltage (4.6 V) and high temperature (80 °C) conditions. More importantly, a 0.4 Ah-level pouch cell demonstrates effective inhibition of thermal runaway under practical mechanical, electrical, and thermal abuse conditions. This work breaks the boundary of electrolyte performance through integrated design and provides a paradigm for developing stable and safe LMBs.

## 2. Results and Discussion

### 2.1. Construction and Properties of Polyfluoride Ionogel Electrolytes

The PFIGE system was formulated through in situ thermal-initiated copolymerization of HFBMA and EGDMA at a precisely regulated molar ratio within a ionic liquid (IL) electrolyte (ILE) comprising 1 M LiTFSI in BMIMTFSI. 2,2'-Azobis(2-methylpropionitrile) (AIBN) initiated polymerization yielded transparent, self-standing membranes (**Figure 2a**), as evidenced by the liquid-to-gel transition in the inset, demonstrating homogeneous phase integration between the fluorinated polymer network and ILE. This PFIGE was directly cast onto Li-Cu composite foils to construct integrated anodes (donated as PFIGE@Li) (Figure 2b). Cross-sectional SEM imaging and elemental mapping analysis revealed a uniform PFIGE thickness of 33 µm, demonstrating excellent conformal coverage of the lithium metal surface while maintaining perfect interfacial integrity (Figure 2c; Figure S1, Supporting Information) Atomic force microscopy (AFM) reveals an ultralow surface roughness (R$_a$ = 2.33 nm, Figure 2d), facilitating intimate electrode-electrolyte contact. Crucially, interfacial adhesion energy reached 132.8 J m$^{-2}$ (Figure 2e), much higher than the baseline (i.e., >5 J m$^{-2}$) for an intimate interface,[27,28] thereby ensuring efficient ion transfer kinetics during battery operation.

Post-polymerization fourier infrared spectroscopy (FTIR) analysis (Figure 2f) confirms complete monomer conversion via disappearance of C=C stretching vibrations (1637 cm$^{-1}$). Deconvolution of C=O stretching modes identify two distinct populations as Li$^+$-coordinated C=O (1730 cm$^{-1}$) and free C=O (1745 cm$^{-1}$). Notably, the 5 cm$^{-1}$ redshift in free C=O relative to precursor solutions indicates strengthened Li$^+$−C=O coordination, consistent with enhanced LiTFSI dissociation.[29,30] Elemental homogeneity is verified through uniform distribution of C/N/O/F/S in the elemental mapping test (Figure S2, Supporting Information), further confirming the high compatibility between the polymer backbone and IL. X-ray photoelectron spectroscopy (XPS) was conducted to resolve the surface chemical environments of PFIGE (Figure S3, Supporting Information). F 1s spectra show characteristic C−F$_x$ bonding

(687.9-689.6 eV), and N 1s peaks corresponding to N atoms in N$^+$ of imidazole rings (400.9 eV)[31] and S−N−S of anions (398.3 eV)[32] in IL.

X-ray diffraction (XRD, Figure S4, Supporting Information) and differential scanning calorimetry (DSC, Figure S5, Supporting Information) reveal an amorphous phase with glass transition temperature (T$_g$) of −40°C, This low T$_g$ results from the plasticizing effect of the IL, which enhances polymer chain mobility, thereby endowing the material with excellent molecular flexibility. This molecular flexibility facilitates molecular migration, enabling self-healing at room temperature. As demonstrated in Figure S6 (Supporting Information), the cut PFIGE sample exhibited self-healing upon contact at room temperature. This self-healing capability arises from the highly reversible and dynamic ion-dipole interactions between the C−F groups of fluoroacrylate and the imidazole cations of BMIMTFSI. Critical evidence emerged from FTIR band shifts. Compared to pure IL, TFSI$^-$ vibrational modes of PFIGE (SO$_2$: 1348 and 1330 cm$^{-1}$; SNS: 1056 cm$^{-1}$; CF$_3$: 1195 cm$^{-1}$) shift to relatively high wavenumbers, indicating weakened anion−cation Coulombic interactions and strengthened F·imidazolium dipole coupling (Figure 2g).[33,34] $^{19}$F nuclear magnetic resonance (NMR) results in Figure 2h demonstrate that the peaks of F atoms in HFBMA move toward relatively low field with the addition of IL and the corresponding intensity decrease, further confirming the presence of ion−dipole interactions.[34]

Density functional theory (DFT) calculations were employed to calculate the highest occupied molecular orbital (HOMO) and lowest unoccupied molecular orbital (LUMO) energies of various compositions. As illustrated in Figure 2i, the HFBMA-EGDMA skeleton molecules exhibit a lower LUMO compared to the organic solvent molecules. This suggests that these molecules are preferentially reduced at the lithium metal anode, contributing to the formation of SEI. In addition, the HFBMA-EGDMA skeleton molecules display a low HOMO energy level. The fluorine atoms in HFBMA-EGDMA possess strong electron-withdrawing capabilities,[35] which endow the skeleton molecules with robust antioxidant properties. Therefore, PFIGE is expected to be highly effective in high-voltage systems to inhibit the surface degradation of active cathode materials at the cathode-electrolyte interface.

### 2.2. Water/Oxygen Shielding Properties of PFIGE

The environmental stability of PFIGE@Li was systematically evaluated through coupled atmospheric exposure tests and molecular-scale simulations. Under ambient air, bare Li surfaces undergo rapid tarnishing within 5 min followed by complete blackening at 30 min, whereas PFIGE@Li maintains metallic luster throughout the test (**Figure 3a**). This exceptional shielding capability originates from two synergistic mechanisms: (i) EGDMA-derived conformal adhesion establishing defect-free Li/electrolyte interfaces, and (ii) fluoropolymer backbone-induced hydrophobicity via trifluoromethyl enrichment at the surface (contact angle = 110°, Figure S7, Supporting Information).[36,37] Practical validation through scaled water immersion tests (Figure 3b) revealed stark contrasts. The unprotected Li-Cu foils exhibited violent exothermic reactions
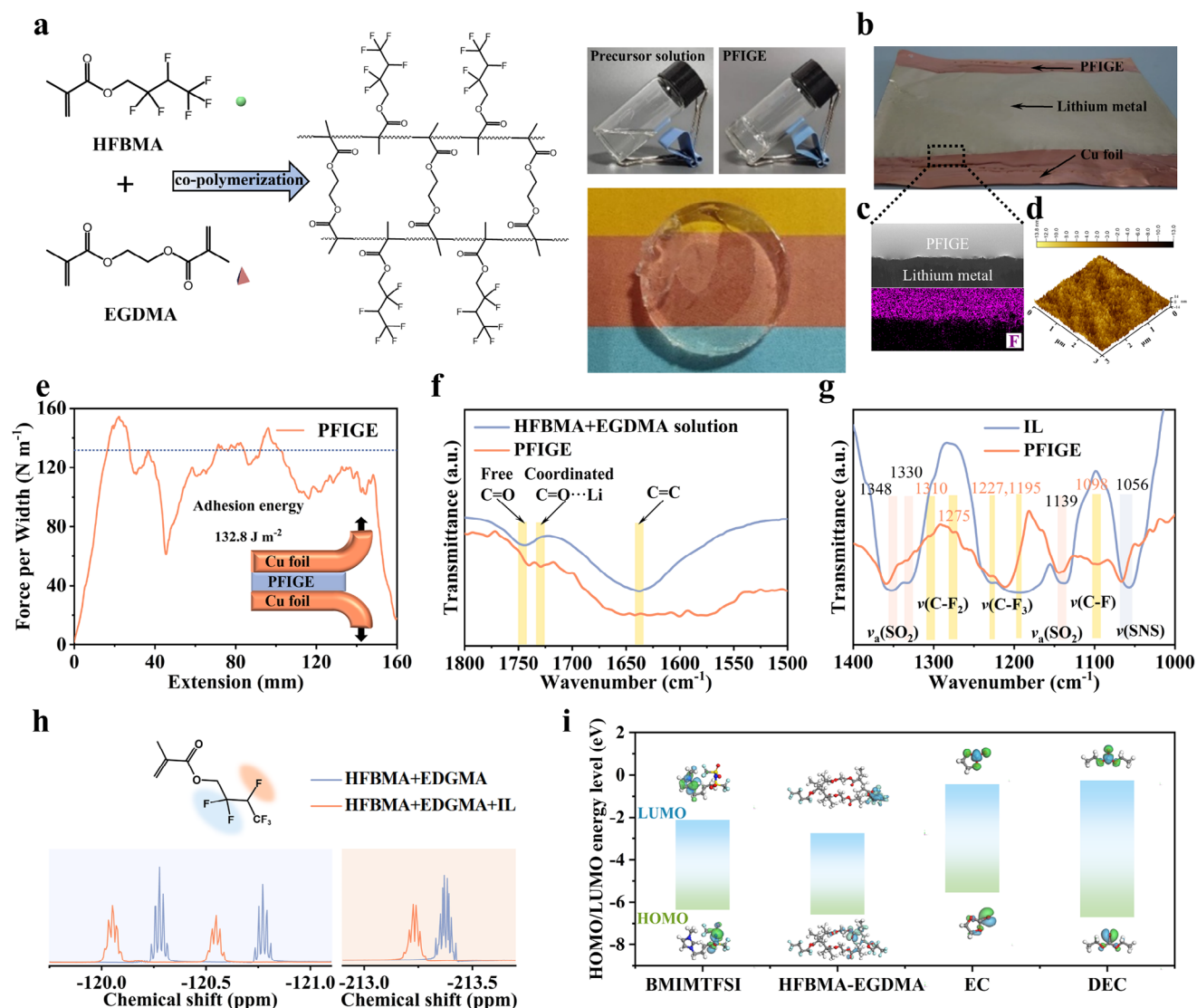
**Figure 2.** a) Synthesis of PFIGE by chemical reaction of HFBMA and EGDMA, and optical photographs before and after synthesis, and demolding. b) Photograph of PFIGE@Li. c) Cross-sectional image of PFIGE@Li and cross-section mapping analysis. d) AFM images of the PFIGE. e) Interfacial adhesion test between the PFIGE and Cu foil. f) and g) FTIR spectra of HFBMA+EGDMA, PFIGE, and IL. h) $^{19}$F NMR spectra of model samples of HFBMA+EGDMA, and HFBMA+EGDMA+IL. (i) HOMO and LUMO energy levels of BMIMTFSI, HFBMA-EGDMA, EC and DEC.

leading to complete lithium corrosion, while PFIGE-coated counterparts demonstrated hermetic isolation with negligible thermal response.

Molecular dynamics (MD) simulations were developed to simulate the wettability of water droplets on PFIGE@Li, focusing on the distribution and diffusion process of water molecule clusters on the PFIGE surface[38] Prior to the analysis, the equilibrium state of water molecules before diffusion was established, as depicted in Figure S8 (Supporting Information). In the adhesion phase shown in Figure 3c, the water droplets on the modeled surface exhibited a hemispherical shape, indicating limited diffusion of water molecules across the PFIGE surface. Notably, no expansion of the water droplets is observed within a 1000 ps timeframe. This suggests that PFIGE effectively acts as a barrier

against water molecules, significantly restricting their diffusion and penetration.

DFT calculations further quantifies and decouples the shielding mechanisms provided by PFIGE. Adsorption energy ($E_{ads}$) analysis (Figure 3d) reveals the PFIGE coating significantly reduced of $H_2O$ and $O_2$ to the lithium surface by 67% (−0.373 eV vs −1.126 eV) and 85% (−1.436 eV vs −9.734 eV), respectively, compared to bare Li(111). This substantial reduction in interfacial interactions fundamentally decreases the sensitivity of the lithium metal surface to water and oxygen molecules.[39] In addition, post-exposure laser microscopy (Figure 3e,f) corroborated these findings. The PFIGE@Li maintains its original surface integrity while bare Li exhibits severe pitting corrosion. These experimental-simulation results highlight the
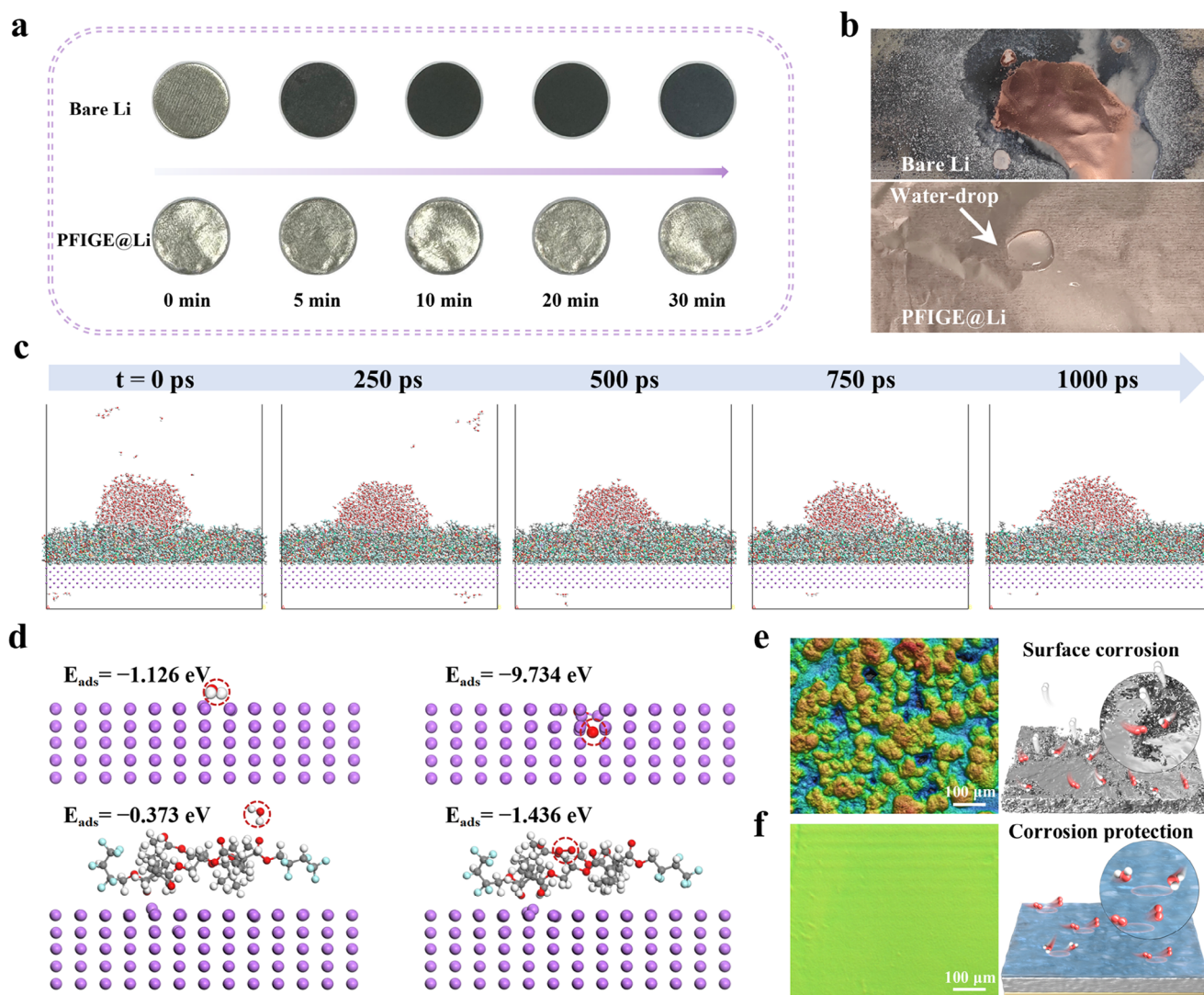
**ADVANCED
SCIENCE NEWS**

www.advancedsciencenews.com

**ADVANCED
FUNCTIONAL
MATERIALS**

www.afm-journal.de

**Figure 3.** a) Optical photographs of bare Li and PFIGE@Li at different exposure times. b) Scaled water immersion tests of bare Li and PFIGE@Li. c) Simulation process of water droplet diffusion on PFIGE@Li surface. d) Atomic conformations and $E_{ads}$ of water and oxygen molecules adsorbed by Li(111) and PFIGE@Li(111). Corresponding surface morphology and corresponding schematic diagram of e) bare Li and (f) PFIGE@Li after erosion by water molecules.

effectiveness of PFIGE in protecting the lithium metal surface from environmental degradation, which is expected to improve the stability, safety, and environmental operability of the lithium metal anode.

### 2.3. Thermal Stability and Flame-Retardant Properties

The thermal stability and flame-retardant properties of PFIGE were systematically evaluated using coupled thermographic and calorimetric analyses. Infrared thermography (**Figure** 4a) revealed significant distinctions in dimensional stability between materials. Traditional polypropylene (PP) separators exhibited progressive curling from 80°C and suffered a molten failure at 140°C, whereas PFIGE maintained its structural integrity up to 300°C. This exceptional thermotolerance is attributed to

the synergistic stabilization between the fluorinated HFBMA-EGDMA network (with a decomposition onset temperature exceeding 300°C as indicated by TGA, Figure 4b) and the heat-resistant BMIMTFSI. Comparative combustion testing against carbonate-based liquid electrolytes (1 M LiPF$_6$ in EC:DEC, referred to as LE) demonstrates PFIGE's intrinsic flame-retardant behavior (Figure 4c), which effectively enhance battery safety under severe conditions.

Cone calorimetry (Figure 4d–g) was used to confirm the superior fire safety of PFIGE. Two crucial metrics for assessing the exothermic behavior and fire safety of materials are the heat release rate (HRR) and total heat release (THR).[40,41] As depicted in Figure 4d,e, PFIGE exhibits notably lower values of both HRR (428 kW m$^{-2}$ vs. 1025 kW m$^{-2}$) and THR (42.43 MJ m$^{-2}$ vs. 77.09 MJ m$^{-2}$) compared to LE. Additionally, the decreased fire growth rate index (FIGRA, calculated as HRR$_{max}$/t$_{HRRmax}$) from 4.15 kW

**ADVANCED
SCIENCE NEWS**

www.advancedsciencenews.com

**ADVANCED
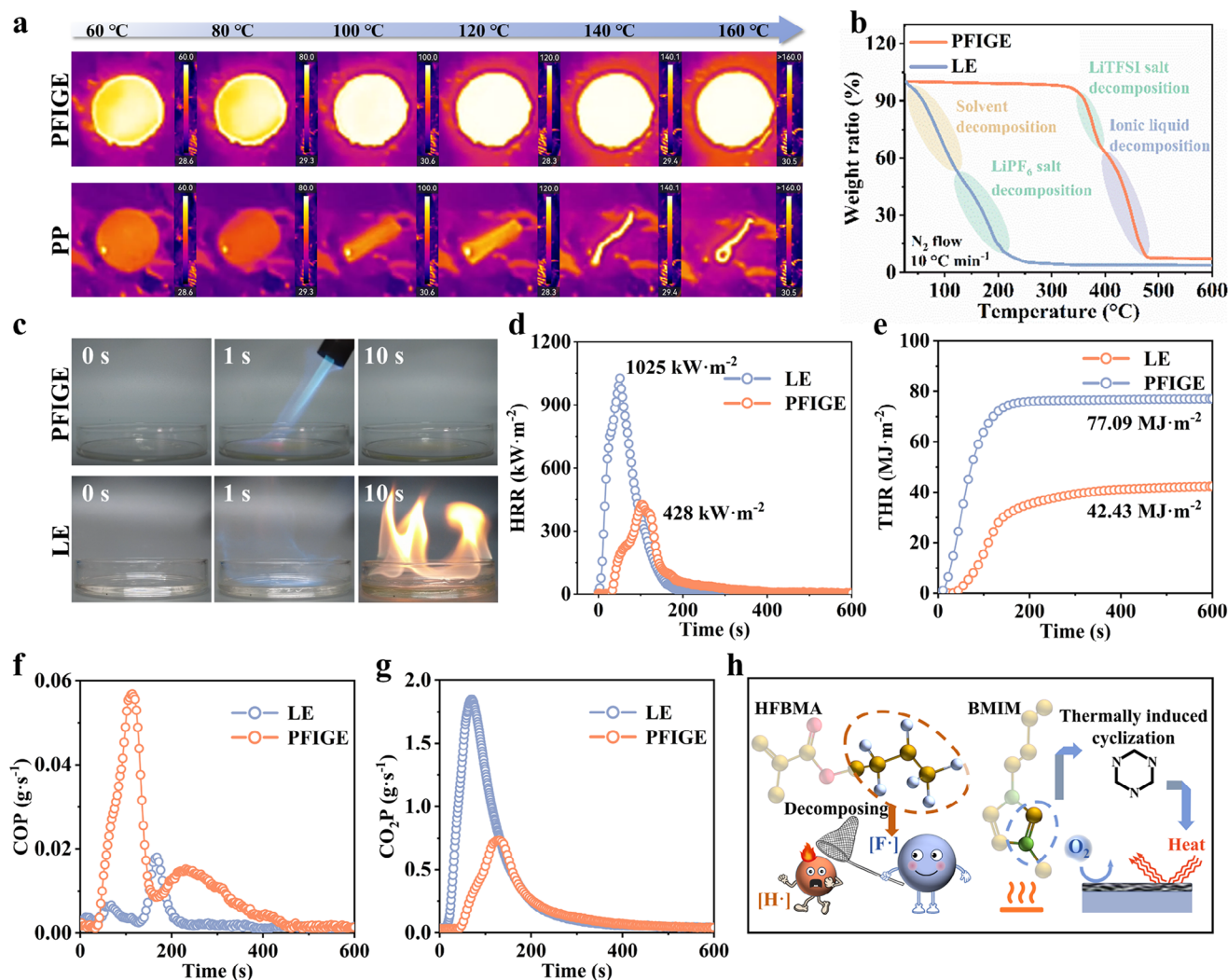FUNCTIONAL
MATERIALS**

www.afm-journal.de

**Figure 4.** a) Infrared thermographic information of PP separators and PFIGE at different temperatures. b) TG curves for LE and PFIGE. c) Combustion tests of LE and PFIGE. d) HRR, e) THR, f) COP, and g) CO$_2$P curves of LE and PFIGE during combustion. h) Flame-retardant mechanism of PFIGE.

m$^{-2}$ s$^{-1}$ to 20.1 kW m$^{-2}$ s$^{-1}$) indicates that PFIGE effectively slows down the spread of fire (Table S1, Supporting Information).[42] The curves for CO production (COP) (Figure 4f) and CO$_2$ production (CO$_2$P) (Figure 4g) illustrate the quantities of gases released during combustion. It is observed that while the CO$_2$P of PFIGE is significantly lower than that of LE, its COP was higher, likely due to incomplete combustion caused by the flame-retardant nature of PFIGE.[43]

Figure 4h elucidates the flame-retardant mechanism of PFIGE. Primarily, the fluorinated polymer matrix releases fluorine radicals (F·) during pyrolysis, which effectively quench chain reaction carriers such as reactive hydrogen radicals (H·) through radical-trapping effects,[14] thereby significantly suppressing the sustained progression of gas-phase combustion reactions. Furthermore, the −CH=N− functional groups undergo thermally induced cyclization reactions under high-temperature conditions, forming six-membered heterocyclic ring compounds containing C−N skeletal structures via self-crosslinking behavior.[44] This in situ carbonization process facilitates rapid formation

of a dense carbonaceous layer. The resultant char layer effectively impedes heat transfer to the material interior while simultaneously obstructing direct oxygen contact with the substrate, thereby establishing dual protective mechanisms at the condensed phase level. The establishment of this gas-phase/condensed-phase synergistic flame-retardant mechanism endows the PFIGE composite with exceptional self-extinguishing characteristics.

### 2.4. Structure-Dependent Regulation of Ion Fluxes

The lithium ion transfer number (tLi$^+$), a critical metric dictating cationic transport dominance, was quantitatively evaluated via Bruce-Vincent-Evans analysis. The PFIGE demonstrates an exceptional tLi$^+$ value of 0.46 (**Figure 5a,b**), surpassing that of liquid counterparts (0.39). This high anion confinement efficacy is attributed to the interaction between fluorinated polymer chains and TFSI$^-$ anions, effectively immobilizing the anions while

**ADVANCED
SCIENCE NEWS**

www.advancedsciencenews.com

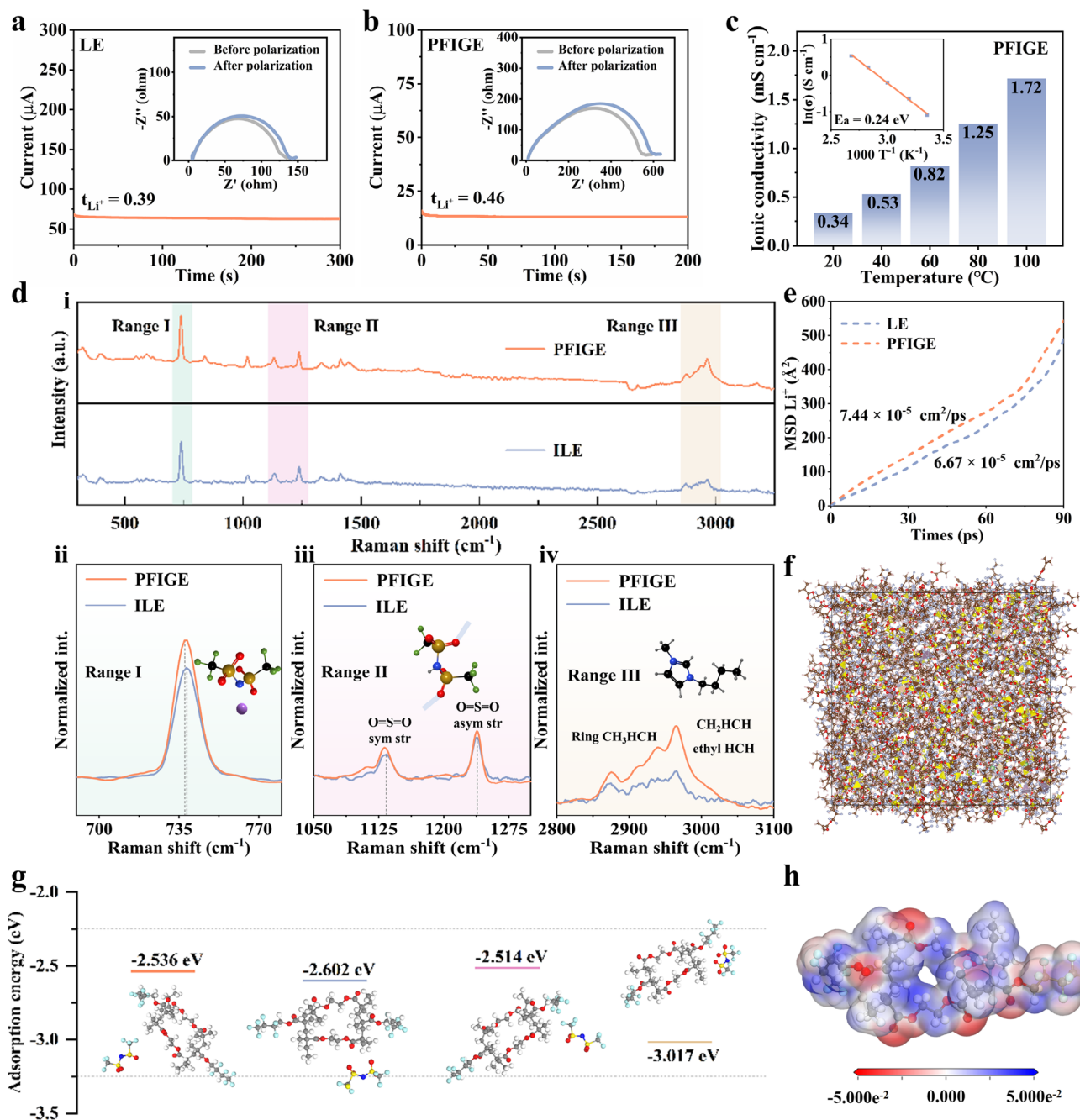**ADVANCED
FUNCTIONAL
MATERIALS**

www.afm-journal.de

**Figure 5.** Polarization curves as well as the initial and steady-state impedance of a) LE and b) PFIGE. c) Arrhenius plot of ionic conductivity of PFIGE. d) i: integrated Raman spectra from ILE and PFIGE, ii~iv: typical enlarged regions corresponding to the ranges in i. MSD of carriers in e) LE and PFIGE as a function of the simulation time. f) MD boxes at equilibrated configurations of PFIGE. g) Interaction strength of the TFSI⁻ anion at different adsorption sites on the HFBMA-EGDMA copolymer. h) ESP of a repeating unit of the HFBMA-EGDMA copolymer.

creating low-barrier Li⁺ conduction pathways.[13] Figure 5c illustrates the Arrhenius dependence of the PFIGE electrolyte's ionic conductivity on temperature, showing an increase from 0.17 mS m⁻¹ (0 °C) to 1.72 mS m⁻¹ (100 °C). The reduced activation energy ($E_a$ = 0.21 eV vs LE's 0.64 eV) supports the advantages of fluorination-induced Li⁺ desolvation (Figure S9, Supporting Information). Additionally, the ultralow electronic conductivity ($1.55 \times 10^{-9}$ S cm⁻¹) shown in Figure S10 (Supporting Informa-

tion) also ensures effective insulation of the PFIGE against electron migration.

To elucidate the ionic conduction mechanisms of the PFIGE, Raman spectroscopy analysis and MD simulations were conducted on PFIGE. As illustrated in Figure 5d, the characteristic Li⁺−TFSI⁻ coordination peak at 740 cm⁻¹ exhibits a distinct redshift in PFIGE relative to ILE, indicating weakened Li⁺−TFSI⁻ coordination strength and enhanced Li⁺ dissociation. This

**ADVANCED
SCIENCE NEWS**

www.advancedsciencenews.com

**ADVANCED
FUNCTIONAL
MATERIALS**

www.afm-journal.de

spectroscopic evidence supports an increased concentration of free Li$^+$ in PFIGE, where the synergistic effects of polar functional groups create optimized coordination pathways, collectively enhancing ionic conductivity. The intensified peak intensity at 740 cm$^{-1}$ (Region I) further confirms higher TFSI$^-$ dissociation efficiency and improved anionic mobility within the polymer matrix. Notably, Region II reveals a shift of the characteristic peaks for O=S=O symmetric stretching (1135 cm$^{-1}$) and O=S=O antisymmetric stretching (1240 cm$^{-1}$) toward lower wave numbers, attributable to hydrogen-bond interactions between TFSI$^-$ oxygen moieties and hydroxyl groups in the HFBMA-EGDMA framework. In Range III, the vibrational modes at 2940 and 2964 cm$^{-1}$ are assigned to ring CH$_3$HCH symmetric stretching, CH$_2$HCH antisymmetric stretching, and ethyl HCH antisymmetric stretching,[45] respectively. A significant increase in the intensity of these vibrational peaks for PFIGE indicates EMIM$^+$ cation liberation from ionic aggregates. Additionally, TFSI$^-$ anions serve as structural bridges between EMIM$^+$ cations and the polymer backbone through electrostatic interactions, spatially confining EMIM$^+$ mobility and thereby creating preferential transport channels for Li$^+$ migration. The mean square displacement (MSD) from MD simulations (Figure 5e,f; Figure S11, Supporting Information) quantitatively validate these mechanisms. As shown in Figure 5e, a enhancement in Li$^+$ diffusion coefficient for PFIGE (7.44 × 10$^{-5}$ cm$^2$ ps$^{-1}$) compared to LE (6.67 × 10$^{-5}$ cm$^2$ ps$^{-1}$). This kinetic superiority arises from the optimized ion transport pathways within the polymer matrix.

DFT calculations were systematically employed to elucidate the anchoring mechanisms of TFSI$^-$ anions within the PFIGE system, focusing on interaction strength quantification between the HFBMA-EGDMA framework and TFSI$^-$. Initially, models representing potential interactions between HFBMA-EGDMA and TFSI anions were constructed (Figure S12, Supporting Information), followed by structural optimization calculations on these representative models. The optimized structural models (Figure 5g) reveal that in the HFBMA molecule, the intermolecular halogen bond formed between the $\sigma$-hole and the N-site of the TFSI$^-$ anion (−3.017 eV) constitutes the strongest chemical interaction within the PFIGE system. Specifically, the halogen atoms in the HFBMA-EGDMA backbone exhibit electrophilic "$\sigma$-holes" along the C−F bond axis, while the N atoms in the TFSI$^-$ anions carry significant negative charges and possess strong nucleophilic properties. This "$\sigma$-hole" can efficiently interact with nucleophilic regions in neighboring molecules,[46,47] thereby forming a stable interaction with the TFSI$^-$ anion. Additionally, hydrogen bonds formed between hydrogen atoms on the EGDMA polymer chain and oxygen atoms on TFSI$^-$ (−2.602 eV), as well as between hydrogen atoms on the EGDMA polymer chain and fluorine atoms on TFSI$^-$ (−2.536 eV), also contribute significantly to limiting the migration of TFSI$^-$. Furthermore, the dipole−dipole coupling effect between the HFBMA-EGDMA backbone and the polar C−F bonds on the TFSI$^-$ anion further aids in restricting anion migration, with an adsorption energy of −2.514 eV. These combined interactions effectively regulate the motional behavior of the TFSI$^-$ anion within the system, ensuring its stability and functionality.

Beyond regulating the mobility of TFSI$^-$ anions, the conformation of the HFBMA-EGDMA backbone critically modulates Li$^+$

coordination and transport dynamics, as elucidated by electrostatic potential (ESP) analysis. Single-point energy calculations for both monomeric and polymeric HFBMA-EGDMA systems reveal distinct ESP distributions (Figure 5h; Figure S13, Supporting Information), with nucleophilic regions (red) localized around O atoms in EGDMA and F/O atoms in HFBMA, while electrophilic zones (blue) dominated fluorinated domains. Notably, after copolymerization to form HFBMA-EGDMA, the F atoms on the polymer chain attract and partially "rob" the electron cloud surrounding the O atoms due to their high electronegativity, resulting in a reduction in the nucleophilicity of these O atoms.[48,49] This electronic perturbation weakens Li$^+$−O coordination strength, thereby lowering the activation energy required for Li$^+$ desorption, as determined by potential energy surface scans. Concurrently, the backbone rigidity is reduced by fluorination, facilitating segmental chain motion and creating dynamic ion transport channels. The synergistic effects of weakened Li$^+$ coordination and enhanced polymer chain mobility significantly reduce Li$^+$ migration barriers, further enhancing the ionic conductivity of the electrolyte.

## 2.5. Anode Stability Assessment and Interface Analysis

The interfacial stability between lithium metal anodes and electrolytes was comparatively analyzed through Li‖Li symmetric cells employing PFIGE and LE. As shown in **Figure 6**a, LE-based cells exhibit a rapid overpotential escalation post-250 h, signaling progressive interface degradation, while PFIGE counterparts maintain ultrastable operation throughout 300 h cycling. SEM characterization of the lithium deposits after cycling (Figure 6b) reveals that the lithium in the LE system exhibits an obvious dendritic structure, directly correlating with heterogeneous Li$^+$ deposition and accelerated SEI failure mechanisms that compromise cyclability and induce internal short-circuit risks. Conversely, PFIGE-enabled systems display densely and smoothly packed Li deposition layers. Notably, the roots of the dendrites tend to form "electrochemical shielding zones," inducing dead lithium and ultimately causing lithium anode failure. Figure S14 (Supporting Information) further demonstrates that the stripped lithium metal in the PFIGE system shows no obvious surface pits, confirming its excellent reversibility during lithium deposition/stripping and improved lithium utilization efficiency. Further analysis through in situ optical microscopy systematically examine the dynamic evolution of lithium deposition behavior. Time-resolved imaging (Figure 6c) reveals rapid dendrite nucleation in LE systems, characterized by moss-like protrusions appearing within 2 min of deposition and continuing to grow during subsequent plating processes. In contrast, PFIGE-enabled deposition demonstrates homogeneous lithium morphology. These results indicate that PFIGE induces a uniform lithium ion flux at the interface, promotes the formation of stable SEI, and achieves uniform lithium deposition.

The electrochemical origin of this optimized lithium deposition behavior was elucidated through characterization of SEI composition and distribution. XPS analysis of cycled lithium metal surfaces reveals distinct compositional differences between the systems. The C 1s spectrum (Figure S15, Supporting Information) demonstrates significantly more organic decomposition products on the LE system surface. Correspondingly,
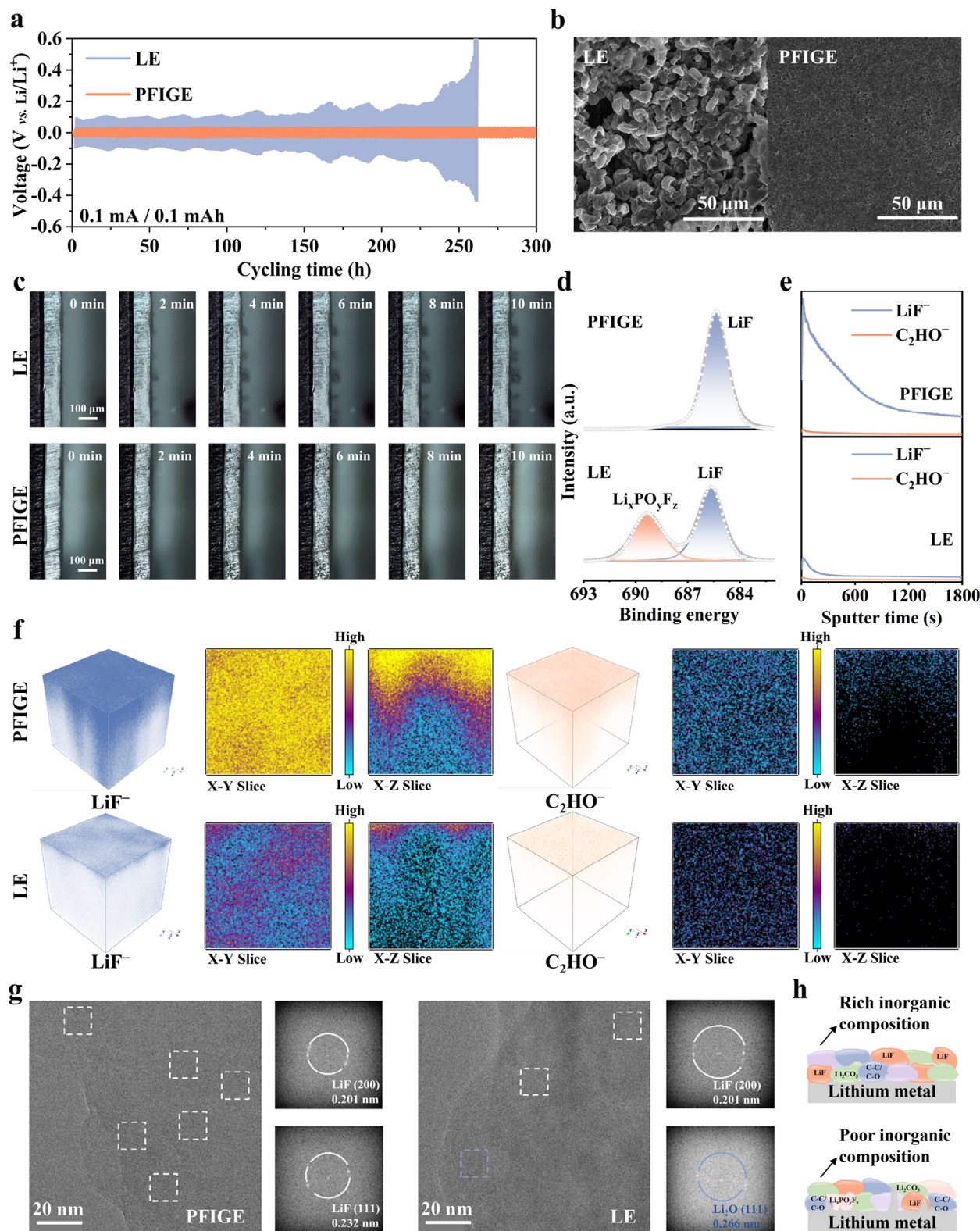
**ADVANCED
SCIENCE NEWS**

www.advancedsciencenews.com

**ADVANCED
FUNCTIONAL
MATERIALS**

www.afm-journal.de

**Figure 6.** a) Cycling performance of Li‖Li cells using LE and PFIGE. b) SEM images of cycled Li using LE and PFIGE-based cells. c) In situ observation of the morphological evolution of electrodeposited Li under a current density of 0.5 mA cm$^{-2}$ with different electrolytes. d) XPS spectra corresponding to F 1s of Li metal after cycling of Li‖Li cells using different electrolytes. e) TOF-SIMS depth profiles of selected fragments on the SEI after cycling. f) TOF-SIMS 3D spatial distribution of LiF$^-$ and C$_2$HO$^-$ fragments, and element mappings in the X-Y and X-Z slices. g) Cryo-TEM images and corresponding localized FFT images of lithium anodes in LE and PFIGE. h)Schematic diagrams of the SEI derived from different electrolytes after cycling.

**ADVANCED
SCIENCE NEWS**

www.advancedsciencenews.com

**ADVANCED
FUNCTIONAL
MATERIALS**

www.afm-journal.de

the F 1s spectrum in Figure 4d reveals an enhancement in LiF content within PFIGE-derived SEI compared to LE counterparts, which is a critical factor conferring superior dendrite suppression due to its high mechanical strength. Additionally, time-of-flight secondary ion mass spectrometry (TOF-SIMS) unveil a stratified SEI architecture in PFIGE systems. As shown in Figure 6e, when using PFIGE, the outer layer of SEI is composed of organic components, while the inner layer is mainly composed of LiF. The fluorine-rich inner layers provide mechanochemical stability, overlain by organic-dominated outer regions that enable dynamic stress dissipation during plating/stripping cycles. Figure 6f displays the 3D structural features obtained from top-down deep sputtering via TOF-SIMS, along with the elemental distribution profiles in the X-Y and X-Z sections. These results clearly demonstrate that the LiF-rich inorganic interfacial layer in the PFIGE system uniformly and completely covers the lithium anode surface. The SEI nanostructures on the lithium anode were further analyzed using cryogenic transmission electron microscopy (Cryo-TEM). The corresponding high-resolution images and fast Fourier transform (FFT) patterns in Figure 6g confirm the dense distribution of inorganic LiF in the PFIGE-derived SEI. Additionally, the electron energy loss spectroscopy (EELS) spectrum of F in Figure S16 (Supporting Information) highlight the comparatively higher LiF content in the inorganic phase. This optimized interfacial structure enhances stability, leading to significant improvements in overall battery performance. As illustrated in Figure 6h, the cycling process leads to the formation of SEIs with low inorganic content for bare Li, whereas the high LiF content in the PFIGE-derived SEI layer contributes to its durability and promotes the homogeneous diffusion of Li$^+$ flow.[50,20] Two key factors have a synergistic effect on the lithium nucleation process, on the one hand, the increase in the Li$^+$ migration significantly reduces concentration polarization, promoting orderly lithium deposition and hindering the growth of lithium dendrites. On the other hand, the electronegative C−F functional group within the polymer backbone establishes strong interactions with Li$^+$ at the interface, attenuating the coordination between Li$^+$ and O atoms. This optimizes the Li$^+$ flux, ultimately ensuring high stability in lithium deposition.

### 2.6. Performance Evaluation of PFIGE in Lithium Metal Batteries

The synergistic coordination between fluorinated polymer frameworks and IL in PFIGE significantly expands its electrochemical stability window to 4.8 V versus 4.4 V for LE (Figure S17, Supporting Information), a critical enabler for high-voltage cathode compatibility. Electrochemical evaluation in Li‖NCM523 configurations demonstrates PFIGE@Li's superior cyclability, achieving 92.1% capacity retention over 300 cycles at 0.5C (2.8−4.3 V) compared to LE's rapid degradation post-100 cycles (**Figure 7a,b**). Even under more demanding conditions at 1C, the PFIGE@Li‖NCM523 cell retains 88.5% of its initial capacity after 100 cycles (Figure S18, Supporting Information). Comparative analysis with previously reported polymer electrolyte systems further confirms the outstanding cycling performance of our PFIGE@Li‖NCM523 configuration, as quantitatively demonstrated in Table S2 (Supporting Information). This enhanced stability stems from PFIGE's oxidation-resistant in-

terfaces, maintaining 78.9% capacity retention at extreme cut-off voltage of 4.6 V (Figure 7c,d) versus LE's failure within 40 cycles. In addition, Figure 7e shows the rate capability of the PFIGE@Li‖NCM523 cell at 0.1−2 C. It shows a satisfactory rate performance and exhibits good reversibility when the current density is restored to 0.1 C. Moreover, PFIGE@Li exhibits extreme temperature resistance, retaining 61.4% capacity after 100 cycles at 80 °C (Figure 7f; Figure S19, Supporting Information). In contrast, LE-based cell suffers from rapid capacity degradation due to the thermal instability and solvent volatility of LE. As a result, PFIGE@Li is able to achieve long cycle stability at both high cut-off voltage and high temperature conditions.

The practical safety and reliability of PFIGE@Li integrated systems were rigorously evaluated through 0.4 Ah-level PFIGE@Li‖NCM523 pouch cells, combining electrochemical cycling with accelerating rate calorimetry (ARC) analysis. Electrochemical profiling demonstrated PFIGE@Li's superior cyclability, achieving 78.7% capacity retention over 50 cycles (**Figure 8a,b**; Figure S20, Supporting Information), which is much higher than that of the LE-based pouch cell. These two pouch cells were subjected to ARC testing for accurate thermal safety analysis. Three characteristic temperatures of $T_1$, $T_2$, and $T_3$ represent the onset temperature of the cells' self-heating reaction (temperature rise rate ≥ 0.02 °C min$^{-1}$), the critical temperature of thermal runaway (temperature rise rate ≥ 1 °C min$^{-1}$), and the maximum temperature of thermal runaway.[16,51] Figure 8c,d shows that the $T_1$, $T_2$ of the pouch cell with PFIGE@Li are significantly higher than that of LE, in which the $T_1$ is 97.7 and 190.3 °C, respectively, which is a 94.8% enhancement, while the $T_2$ is 139.8 and 225.6 °C, respectively, which is a 61.4% enhancement, and furthermore, the characteristic temperature of $T_3$ of the PFIGE@Li-based cell is reduced by 28.8% compared with that of LE-based cell (402.1 °C vs 286.3 °C). More importantly, the thermal runaway induction period is extended from 1200 mins in LE to 3050 mins in PFIGE@Li, indicating that the use of PFIGE can effectively delay thermal runaway.

The practical safety of PFIGE@Li-based cells was rigorously validated through multi-condition abuse tests. In the thermal stability evaluation (Figure 8e), a fully charged PFIGE@Li-based cell was subjected to an extreme heating protocol (130 °C for 30 min). Remarkably, the cell temperature consistently tracked the ambient temperature with a slight hysteresis and remained stable without explosion or fire upon cooling. Furthermore, nail penetration tests under simulated internal short-circuit conditions (Figure 8f) demonstrated effective thermal runaway mitigation, with the PFIGE@Li cell showing no detectable temperature rise or hazardous gas release post-penetration. Crucially, combustion tests (Figure 8g) confirmed the intrinsic non-flammability of PFIGE@Li cells, as evidenced by zero ignition during direct flame exposure. In stark contrast, conventional LE-based cells exhibited immediate ignition and sustained combustion under identical conditions.

The evolution of gaseous byproducts in operational pouch cells were systematically monitored to evaluate interfacial stability and safety risks, with PFIGE demonstrating exceptional suppression of electrochemical side reactions. As can be seen in Figure 8h, gas chromatography-mass spectrometry (GC-MS) quantification reveals a large amount of H$_2$ and C$_x$H$_y$ gases are
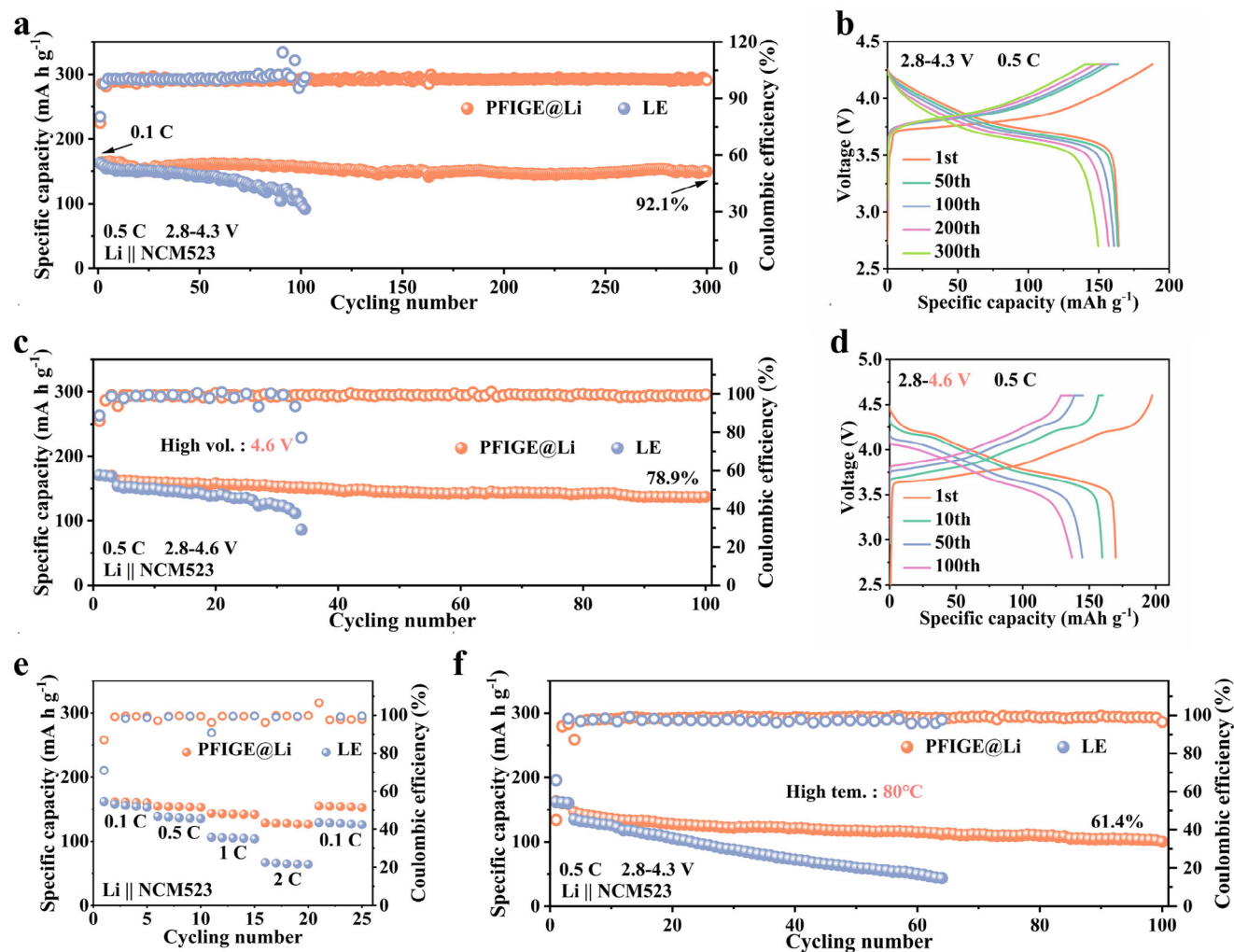
**Figure 7.** a) Cycling performance for Li||NCM523 cells using with LE and PFIGE@Li at 0.5 C. b) Charge/discharge curves of PFIGE@Li||NCM523 cell. c) Cycling performance of Li||NCM523 cells at 4.6 V. d) Charge/discharge curves of PFIGE@Li||NCM523 cell at 4.6 V. e) Rate performance of Li||NCM523 cells with LE and PFIGE@Li. f) Cycling performance for Li||NCM523 cells with LE and PFIGE@Li at 80 °C.

generated in the LE-based cell during the cycling period, whereas only a very small amount of such gases are released in the PFIGE@Li-based cell under the same conditions. It is suggested that the design of PFIGE@Li contributes to the interfacial stability and ultimately inhibits electrolyte decomposition and gas release during battery cycling. To further verify the safety of the PFIGE@Li||NCM523 pocuh cell, more stringent electric drill and saw damage tests were carried out. As shown in Figure 8i, the results show that under these conditions, the PFIGE@Li pocket cell can still maintain a normal open-circuit voltage without the risk of smoke, combustion, or explosion. In summary, these series of rigorous tests demonstrate that PFIGE@Li can effectively reduce gaseous safety hazards and catastrophic failure modes in LMBs.

## 3. Conclusion

In conclusion, a molecular-level integrated strategy presented in this work demonstrates a approach to addressing the instabil-

ity and safety concern of lithium metal anodes. By orchestrating the dynamic interplay between a fluorinated polymer matrix and ionic liquid components, the PFIGE system establishes a dual-functional architecture that simultaneously mitigates interfacial degradation and external hazards. The coordination of C−F groups and TFSI⁻ anions not only establishes a robust barrier against ambient corrosion but also promotes ion transport kinetics, thereby homogenizing lithium nucleation patterns and suppressing dendrite growth. Moreover, the self-adaptive ion−dipole interactions within the electrolyte framework enable damage resilience during prolonged cycling, while its thermally decomposition mechanism introduces an inherent safety protocol. The exceptional performance retention of full cells under extreme operational conditions, coupled with the successful suppression of thermal runaway in practical pouch-cell configurations, validates the viability of this molecularly engineered ionogel as a universal electrolyte platform. This paradigm-shifting electrolyte establishes an approach for advancing next-generation energy storage systems.
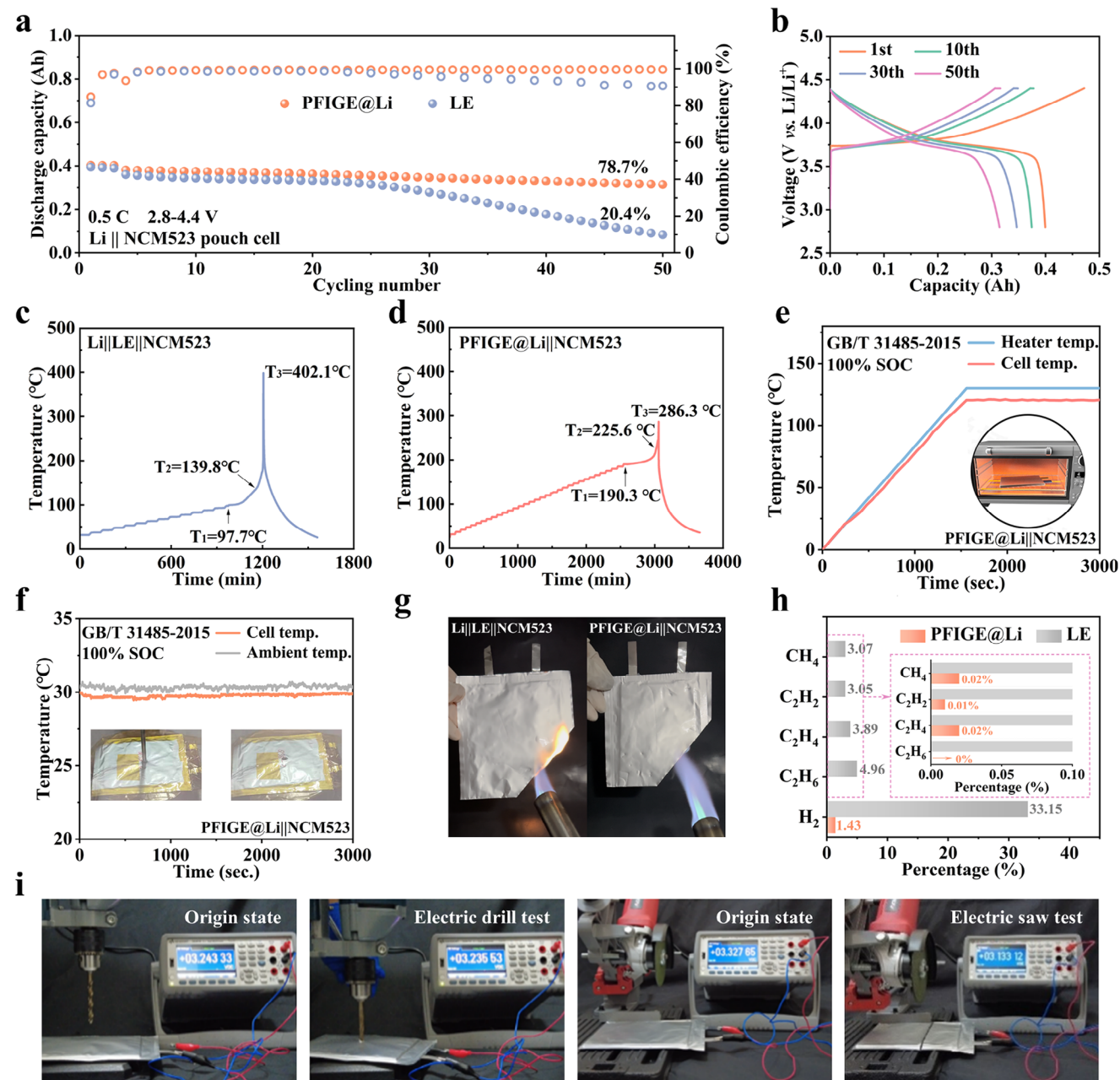
ADVANCED
SCIENCE NEWS

www.advancedsciencenews.com

ADVANCED
FUNCTIONAL
MATERIALS

www.afm-journal.de

**Figure 8.** a) Cycling performance of Li||NCM523 pouch cells with LE and PFIGE@Li. b) Charge-discharge curve of PFIGE@Li||NCM523 pouch cell. Thermal runaway temperature plots of fully-charged pouch cells with c) LE and d) PFIGE@Li. e) Heating test and f) nail penetration test of fully-charged pouch cell with PFIGE@Li. g) Ignition tests of two pouch cells. h) Types and contents of gases produced in two pouch cells. (i) Open-circuit voltage of the PFIGE@Li||NCM523 cell before and after electric drill and saw damage tests.

## 4. Experimental Section

*Materials*: 2,2,3,4,4,4-Hexafluorobutyl acrylate (HFBA, >95%), ethylene glycol dimethacrylate (EGDMA, >98%), 2,2′-Azobis(2-methylpropionitrile) (AIBN, 98%), 1-Butyl-3-methylimidazolium bis(trifluoromethylsulfonyl)imide ([BMIMTFSI, 98%) were purchased from Aladdin, Lithium bis(trifluoromethanesulfonyl)imide (LiTFSI, 99.8%) was purchased from DodoChem. If not particularly indicated, all other reagents were purchased from commercial sources and used without further purification.

*Electrolyte Preparation*: The hydrophobic ionogel electrolyte was prepared by the following method: First, 40wt.% monomer (HFBMA), 0.1wt.% crosslinker (EGDMA), 60wt.% ionic liquid (BMIMTFSI), 1 M LiTFSI (versus ionic liquid), and 0.1wt.% thermal initiator (AIBN) was dispersed to prepare a precursor solution. Then, the PFIGE was formed by thermal-initiation polymerization at 60 °C for 90 mins.

*Characterizations*: The morphologies and mappings were obtained by field-emission scanning electron microscopy (FE-SEM, Nova NANOSEI 450). Surface topography and roughness were obtained from Atomic Force Microscope (AFM, Bruker Dimension Icon). Contact angle tests were

carried out on an JY-82C contact angle measuring instrument. Surface chemical compositions of solid film samples were characterized by an x-ray photoelectron spectroscopy (XPS, Thermo ESCALAB 250XI) and time-of-flight secondary ion mass spectrometry (TOF-SIMS, TOF.SIMS5 IONTOF GmbH). The $^{19}$F nuclear magnetic resonance spectra were determined on a Bruker 600 MHz NMR spectrometer using DMSO as solvent. Attenuated total reflection Fourier transform infrared (ATR-FTIR) spectroscopy was carried out on a Thermo Scientific Nicolet 6700 infrared spectrophotometer in the range of $4000-525$ cm$^{-1}$. X-ray diffraction (XRD) patterns were recorded on a Ultima IV diffractometer X-ray diffractometer with Cu K$_\alpha$ radiation ($\lambda = 1.5406$ Å). Adhesion energy measurements were performed using a universal testing machine (INSTRON 5982). Differential scanning calorimetry (DSC) measurements were measured on a TA DSC25 from $-70$ to 25 °C at a heating rate of 10 °C min$^{-1}$ under a nitrogen atmosphere. Thermal gravimetric analysis (TGA) measurements were performed on a Rigaku TG/DTA8122 from 25 to 600 °C at a ramping rate of 10 °C min$^{-1}$ under a nitrogen atmosphere. Infrared thermal images were taken by a FLIR C5 thermal imager. Laser microscope images were recorded by KEYENCE VK-X150 at 25 °C.

*Electrode Preparation and Battery Assembly*: The NMC523 cathode was prepared using a slurry casting process. First, the active material (NMC523), conductive agent (Super P), and binder polyvinylidene fluoride (PVDF) were dispersed in N-methyl-2-pyrrolidone (NMP) solvent in a mass ratio of 8:1:1. After stirring for 6 h, a homogeneous slurry was formed. This slurry was then uniformly coated onto aluminum foil current collectors. The coated electrode sheets were transferred to a vacuum drying oven and dried at 80 °C for 24 h to completely remove any residual solvent. The PFIGE precursor solution was cast onto a lithium-copper composite foil (lithium metal thickness: 50 μm). After coating, the slurry was smoothed using a coater. The integrated anode was then constructed by heating the coated foil in an oven at 80 °C for 90 min. Li||NCM523 cells were assembled in an argon protected glove box (H$_2$O/O$_2$ < 0.1 ppm) using a CR2025-type stainless steel cases, and without the addition of a separator for the PFIGE@Li based battery assembly process.

*Electrochemical Measurements*: All electrochemical measurements were performed on a CHI660E electrochemical workstation. The sandwiched stainless steel (SS)||electrolyte||SS type blocking electrode system to obtain electrochemical impedance spectroscopy (EIS) data with frequency from $0.1-10^6$ Hz (amplitude: 5 mV). The electronic conductivity ($\gamma$) of the electrolyte was calculated through the polarization current time curve. Measurement system: SS||electrolyte||SS blocking electrode system. 1 V polarized voltage is applied to the test electrode and the change of current with time can be monitored. The $\gamma$ was determined according to Ohm's law, $\gamma = \frac{I_{ss} \cdot L}{U \cdot S}$, where $\sigma$ is the electronic conductivity, L is the thickness of the electrolyte, S is the area of the electrolyte, U is the polarization voltage, and I$_{ss}$ is the steady-state current. The transference number (tLi$^+$) was determined by a combined method of AC impedance spectroscopy and DC polarization (10 mV) using a Li||electrolyte||Li symmetrical cell. The electrochemical stability window was evaluated via linear sweep voltammetry (LSV) ranging from 0 to 6 V at a scan rate of 1 mV s$^{-1}$ using a Li||electrolyte||SS two-electrode cell.

*Computational Methods*: The HOMO and LUMO energy levels were calculated using the DMol3 module. Wettability of water droplets on the PFIGE-Li surface and ionic conduction in different electrolytes were simulated using the Forcite-Dynamics module with molecular dynamics. The details of the calculations are in the Supporting Information document.

## Supporting Information

Supporting Information is available from the Wiley Online Library or from the author.

## Acknowledgements

## Conflict of Interest

The authors declare no conflict of interest.

## Author Contributions

T.L. was responsible for conceptualization, visualization, methodology, and writing of the original draft. Anjun Hu contributed to the investigation and writing through review and editing. Y.L. carried out formal analysis and validation. Borui Yang and Kun Li both contributed to conceptualization and visualization. Kai Chen was involved in formal analysis and visualization. Jingyun Jiang and Fei Li conducted formal analysis and validation. Z.W.S. contributed through funding acquisition, formal analysis, and validation. Jian Wang also participated in formal analysis and validation. Jianping Long contributed to writing through review and editing, and was responsible for funding acquisition, project administration, and supervision.

## Data Availability Statement

The data that support the findings of this study are available in the supplementary material of this article.

## Keywords

[1] Q. Xu, T. Li, Z. Ju, G. Chen, D. Ye, G. I. N. Waterhouse, Y. Lu, X. Lai, G. Zhou, L. Guo, K. Yan, X. Tao, H. Li, Y. Qiu, *Nature* **2025**, *637*, 339.

[2] W. Zhang, Z. Wang, H. Wan, A.-M. Li, Y. Liu, S.-C. Liou, K. Zhang, Y. Ren, C. Jayawardana, B. L. Lucht, C. Wang, *Nat. Mater.* **2025**, *24*, 414.

[3] S. Yang, J. Hu, F. Jiang, H. Yuan, H. S. Park, J. Huang, *InfoMat* **2024**, *6*, 12512.

[4] Y. Li, X. Feng, G. Yang, W. Y. Lieu, L. Fu, C. Zhang, Z. Xing, M.-F. Ng, Q. Zhang, W. Liu, J. Lu, Z. W. Seh, *Nat. Commun.* **2024**, *15*, 9364.

[5] B. Yang, A. Hu, T. Li, K. Li, Y. Li, J. Jiang, Z. Xiao, Z. W. Seh, J. Long, *Energy Storage Mater.* **2024**, *70*, 103512.

[6] K. Zhang, F. Wu, X. Wang, S. Weng, X. Yang, H. Zhao, R. Guo, Y. Sun, W. Zhao, T. Song, X. Wang, Y. Bai, C. Wu, *Adv. Energy Mater.* **2022**, *12*, 2200368.

[7] C. Chen, J. Zhang, J. Hu, Q. Liang, X. Xiong, *Nat. Commun.* **2023**, *14*, 4018.

[8] Y. Wang, Z. Wang, L. Zhao, Q. Fan, X. Zeng, S. Liu, W. K. Pang, Y. He, Z. Guo, *Adv. Mater.* **2021**, *33*, 2008133.

[9] X. Duan, Y. Li, K. Huang, S. Tu, G. Li, W. Wang, H. Luo, Z. Chen, C. Li, K. Cheng, X. Wang, L. Wang, Y. Sun, *Sci. Bulletin* **2025**, *70*, 914.

[10] Y. Li, E. Mao, Z. Min, Z. Cai, Z. Chen, L. Fu, X. Duan, L. Wang, C. Zhang, Z. Lu, W. Liu, Z. W. Seh, Y. Sun, *ACS Nano* **2023**, *17*, 19459.

[11] L. Wang, J. Guo, Q. Qi, X. Li, Y. Ge, H. Li, Y. Chao, J. Du, X. Cui, *Nano-Micro Lett.* **2025**, *17*, 111.

[12] A. Hu, W. Chen, X. Du, Y. Hu, T. Lei, H. Wang, L. Xue, Y. Li, H. Sun, Y. Yan, J. Long, C. Shu, J. Zhu, B. Li, X. Wang, J. Xiong, *Energy Environ. Sci.* **2021**, *14*, 4115.

[13] S. Wang, S. Xiao, S. Li, C. Liu, H. Cai, W. Sun, Z. Huang, W. Lai, *Angew. Chem., Int. Ed.* **2024**, *63*, 202412434.

[14] A. Hu, W. Chen, F. Li, M. He, D. Chen, Y. Li, J. Zhu, Y. Yan, J. Long, Y. Hu, T. Lei, B. Li, X. Wang, J. Xiong, *Adv. Mater.* **2023**, *35*, 2304762.

[15] T. Li, K. Chen, B. Yang, K. Li, B. Li, M. He, L. Yang, A. Hu, J. Long, *Chem. Sci.* **2024**, *15*, 12108.

[16] B. Yang, Y. Pan, T. Li, A. Hu, K. Li, B. Li, L. Yang, J. Long, *Energy Storage Mater.* **2024**, *65*, 103124.

[17] X. Hu, J. Yu, Y. Wang, W. Guo, X. Zhang, M. Armand, F. Kang, G. Wang, D. Zhou, B. Li, *Adv. Mater.* **2024**, *36*, 2308275.

[18] H. Li, F. Zhang, W. Wei, X. Zhao, H. Dong, C. Yan, H. Jiang, Y. Sang, H. Chen, H. Liu, S. Wang, *Adv. Energy Mater.* **2023**, *13*, 2301023.

[19] Y. Zang, P. Peng, F. Pei, R.-H. Li, L. Wu, D.-Q. Lu, Y. Zhang, K. Huang, Y. Shen, Y.-H. Huang, Y.-Q. Lan, *Natl. Sci. Rev.* **2025**, *12*, nwae443.

[20] H. Huang, S. Liu, Y. Xie, J. Liu, C. Shi, M. Sun, H. Peng, J. Lan, Y.-P. Deng, L. Huang, S.-G. Sun, *J. Am. Chem. Soc.* **2024**, *146*, 31137.

[21] Y. Chen, Z. Ma, Y. Wang, P. Kumar, F. Zhao, T. Cai, Z. Cao, L. Cavallo, H. Cheng, Q. Li, J. Ming, *Energy Environ. Sci.* **2024**, *17*, 5613.

[22] R. Xu, A. Hu, Z. Wang, K. Chen, J. Chen, W. Xu, G. Wu, F. Li, J. Wang, J. Long, *J. Energy Chem.* **2025**, *105*, 35.

[23] J. Cao, W. Chen, A. Gao, D. Muhtar, G. Du, G. Qian, X. Lu, F. Xie, Y. Sun, X. Lu, *Angew. Chem., Int. Ed.* **2025**, *137*, 202413065.

[24] X. You, Y. Feng, D. Ning, H. Yao, M. Wang, J. Wang, B. Chen, G.-H. Zhong, C. Yang, W. Wu, *Nano Lett.* **2024**, *24*, 11367.

[25] Z. Wang, C. Zhao, N. Yao, Y. Lu, Z. Xue, X. Huang, P. Xu, W. Huang, Z. Wang, J. Huang, Q. Zhang, *Angew. Chem., Int. Ed.* **2025**, *64*, 202414524.

[26] X. Cui, J. Yang, Z. Xu, Q. Liu, Y. Nuli, J. Wang, *Nano Energy* **2022**, *95*, 107013.

[27] M. J. Lee, J. Han, K. Lee, Y. J. Lee, B. G. Kim, K.-N. Jung, B. J. Kim, S. W. Lee, *Nature* **2022**, *601*, 217.

[28] J. Li, A. D. Celiz, J. Yang, Q. Yang, I. Wamala, W. Whyte, B. R. Seo, N. V. Vasilyev, J. J. Vlassak, Z. Suo, D. J. Mooney, *Science* **2017**, *357*, 378.

[29] Y. Wu, P. Yu, T. Dong, L. Wang, H. Xu, J. Wang, X. He, *Mater. Today* **2025**, *83*, 223.

[30] H. Wang, X. Li, Q. Zeng, Z. Li, Y. Liu, J. Guan, Y. Jiang, L. Chen, Y. Cao, R. Li, A. Wang, Z. Wang, L. Zhang, *Energy Storage Mater.* **2024**, *66*, 103188.

[31] Y. Ren, Z. Liu, G. Jin, M. Yang, Y. Shao, W. Li, Y. Wu, L. Liu, F. Yan, *Adv. Mater.* **2021**, *33*, 2008486.

[32] K. Forster-Tonigold, J. Kim, J. Bansmann, A. Groß, F. Buchner, *ChemPhysChem* **2021**, *22*, 441.

[33] X. Ming, J. Du, C. Zhang, M. Zhou, G. Cheng, H. Zhu, Q. Zhang, S. Zhu, *ACS Appl. Mater. Interfaces* **2021**, *13*, 41140.

[34] P. Shi, Y. Wang, W. W. Tjiu, C. Zhang, T. Liu, *ACS Appl. Mater. Interfaces* **2021**, *13*, 49358.

[35] Z. Yu, P. Wu, *Adv. Mater.* **2021**, *33*, 2008479.

[36] Z. Kong, E. K. Boahen, D. J. Kim, F. Li, J. S. Kim, H. Kweon, S. Y. Kim, H. Choi, J. Zhu, W. Bin Ying, D. H. Kim, *Nat. Commun.* **2024**, *15*, 2129.

[37] Q. Nian, X. Luo, D. Ruan, Y. Li, B.-Q. Xiong, Z. Cui, Z. Wang, Q. Dong, J. Fan, J. Jiang, J. Ma, Z. Ma, D. Wang, X. Ren, *Nat. Commun.* **2024**, *15*, 4303.

[38] H. Jeong, B. Kim, T. Park, S. Yoo, S. K. Nam, *Surfaces and Interfaces* **2022**, *35*, 102463.

[39] J. Luo, Q. Huang, D. Shi, Y. Qiu, X. Zheng, S. Yang, B. Li, J. Weng, M. Wu, Z. Liu, Y. Yu, C. Yang, *Adv. Funct. Mater.* **2024**, *34*, 2403021.

[40] L. Han, C. Liao, Y. Liu, H. Yu, S. Zhang, Y. Zhu, Z. Li, X. Li, Y. Kan, Y. Hu, *Energy Storage Mater.* **2022**, *52*, 562.

[41] S. Zhang, L. Huang, C. Zhang, Q. Lv, Z. Wu, J. Lai, L. Wang, C. Li, *Energy Storage Mater.* **2024**, *71*, 103581.

[42] X.-C. Jiang, P. Li, Y. Liu, J.-S. Wang, *Cellulose* **2023**, *30*, 1321.

[43] Y. Yang, J. Lyu, J. Chen, J. Liao, X. Zhang, *Adv. Funct. Mater.* **2021**, *31*, 2102232.

[44] Q. Zhao, X. Liu, S. Deng, X. Zheng, B. Zeng, X. Liu, Y. Xu, C. Yuan, L. Dai, *Chem. Eng. J.* **2024**, *495*, 153283.

[45] J. Sun, C. He, Y. Li, Q. Zhang, C. Hou, M. De Volder, K. Li, H. Wang, *Energy Storage Mater.* **2023**, *54*, 40.

[46] C. Wang, H. Liu, Y. Liang, D. Li, X. Zhao, J. Chen, W. Huang, L. Gao, L. Fan, *Adv. Funct. Mater.* **2023**, *33*, 2209828.

[47] W. Lin, Y. Zhang, Y. Zhang, K. Ji, M. Chen, *ACS Appl. Mater. Interfaces* **2024**, *16*, 27439.

[48] H. Peng, T. Long, J. Peng, H. Chen, L. Ji, H. Sun, L. Huang, S. Sun, *Adv. Energy Mater* **2024**, *14*, 2400428.

[49] S. Qi, M. Li, Y. Gao, W. Zhang, S. Liu, J. Zhao, L. Du, *Adv. Mater.* **2023**, *35*, 2304951.

[50] Z. Wang, C. Su, R. Xu, K. Li, B. Yang, T. Li, K. Chen, W. Xu, J. Chen, F. Li, B. Li, A. Hu, J. Long, *Energy Storage Mater.* **2025**, *75*, 104105.

[51] R. Chen, A. M. Nolan, J. Lu, J. Wang, X. Yu, Y. Mo, L. Chen, X. Huang, H. Li, *Joule* **2020**, *4*, 812.